CFD Analysis of Arc–Flow Interaction in a High-Voltage Gas Circuit Breaker Using an Overset Method

Jung Ho Park, *Student Member, IEEE,* Kyu Hong Kim, Chang Ho Yeo, and Hong Kyu Kim

Abstract—A computational analysis of the gas flow in a gas circuit breaker is presented in this paper. A structured grid with a high-order conservative overset method is used for an accurate flow analysis. In addition, this paper includes the modeling of the arc, radiation, and ablation of the nozzle. The results of the flow analysis are compared with the experimental data, showing good agreement with the experimental data.

Index Terms—Ablation, gas circuit breaker (GCB), radiation, structured grid.

I. INTRODUCTION

HIGH-PRESSURE gas circuit breaker (GCB) is one of the most competitive components among all the circuit breakers. Given that the value of the global market is expected to increase to a great extent, the importance of research in this area will also increase with the arrival of the Information technology (IT) age and the replacement of power transmission plants. The flow in a high-voltage GCB includes complicated physics such as arc or plasma. Therefore, an accurate analysis of the internal flow of a GCB is difficult but an accurate analysis is crucial for a precise prediction of the performance of a GCB. Generally, there are two ways to analyze the flow in a GCB, an experimental test and using a computational fluid dynamics (CFD) analysis. From an experiment, the overall flow patterns and flow values at the arbitrary points are difficult to know because the data can only be acquired at the particular points. Therefore, a flow analysis from an experiment is restricted, making CFD analysis very important.

A CFD analysis using an unstructured grid system with a grid regeneration technique is widely used to analyze the internal flow inside a circuit breaker. However, it is known that CFD code based on a structured grid has the advantages of accuracy compared with an unstructured grid, especially in the boundary layer [18]. In addition, unstructured grid method has higher memory requirements than the structured grid method [18]. For this reason, a flow analysis using a structured grid system with third-order spatial accuracy is used in this paper Generally, it is difficult to represent complicated shapes such as the shape of two electrodes inside a GCB with a structured type grid. To resolve this problem, a fourth-order conservative overset method is used to represent a curve-shaped electrode and a nozzle as well as the motion of the moving parts with a structured grid. AUSMPW+ flux difference scheme [1], [2] with third-order Multi-dimensional Limiting Process [3] and lower-upper symmetric Gauss-Seidel (LU-SGS) time integration schemes [4], [5] is used to analyze an internal gas flow. In addition, an electric field analysis combined with nozzle ablation is considered to gain an accurate solution. To calculate the radiative source term and the radiative heat flux at the ablating wall, P-1 approximation is used. P-1 approximation simplifies radiative transfer equation (RTE) with an elliptic-type equation, and the methods for solving simple elliptic-type equations are well known. However, using the central difference method in a region with a high-gradient temperature can lead to an unstable result. A new difference method that can be used to solve electric potential equations and P-1 approximation is introduced. The proposed method relies on smoothly changing function to construct a diagonal dominant matrix based on the gradient of the absorption coefficient.

Overall, the analysis using structured grid with an overset method has been done with high-order accuracy. This analysis program will be widely used to verify the performance of a breaker before experimentation and production. A flow simulation will help make GCBs smaller on the drawing board while also providing very accurate flow data.

II. GOVERNING EQUATIONS

A local thermal equilibrium (LTE) assumption for a SF_6 gas is included in the computation. The governing equation is a 2-D axisymmetric Navier–Stokes equation. An energy source term from to account for Joule heating and radiation is included in the RHS of the equations. An ablating particle is

also considered in this analysis and therefore, the continuity equation of the particle is added. Diffusion of the ablated particle is neglected in this paper.

The conservative form of an axisymmetric Navier–Stokes equation is as follows:

$$\frac{\partial Q}{\partial t} + \frac{\partial E}{\partial x} + \frac{\partial F}{\partial y} + H = \frac{\partial E_v}{\partial x} + \frac{\partial F_v}{\partial y} + H_v + S \quad (1)$$

where the flux and source terms are described as follows:

$$Q = \begin{pmatrix} \rho \\ \rho u \\ \rho v \\ \rho e_t \\ \rho_{ptfe} \end{pmatrix} \quad E = \begin{pmatrix} \rho u \\ \rho u^2 + p \\ \rho uv \\ (\rho e_t + p)u \\ \rho_{ptfe}u \end{pmatrix}$$

$$F = \begin{pmatrix} \rho v \\ \rho vu \\ \rho v^2 + p \\ (\rho e_t + p)v \\ \rho_{ptfe}v \end{pmatrix} \quad H = \frac{1}{y} \begin{pmatrix} \rho v \\ \rho vu \\ \rho v^2 \\ (\rho e_t + p)v \\ \rho_{ptfe}v \end{pmatrix}$$

$$E_v = \begin{pmatrix} 0 \\ \tau_{xx} \\ \tau_{xy} \\ u\tau_{xx} + v\tau_{xy} + k\frac{\partial T}{\partial x} \\ 0 \end{pmatrix} \quad F_v = \begin{pmatrix} 0 \\ \tau_{xy} \\ \tau_{yy} \\ u\tau_{xy} + v\tau_{yy} + k\frac{\partial T}{\partial y} \\ 0 \end{pmatrix}$$

$$S = \begin{pmatrix} 0 \\ 0 \\ 0 \\ S_{\text{ohm}} - S_{\text{rad}} \\ 0 \end{pmatrix}.$$

In the above equations, ρ is the total density of the gas mixture, ρ_{ptfe} is the density of polytetrafluoroethylene (PTFE), the energy S_{ohm} is the energy source term by Joule heating, and S_{rad} is the energy source term by radiation. Source terms are calculated by solving the electric potential equation and the RTE. The electric potential equation is expressed as (2). From (3), the scaling factor V can be obtained using the current obtained from an experiment and the gradient of the electric potential, which is computed using (2). The electric field and Joule heating term can be calculated from the scaling factor V

$$\nabla \cdot (\sigma \nabla \Phi) = 0. \quad (2)$$
$$\vec{E} = -V\nabla\Phi \quad \vec{J} = -\sigma \cdot \vec{E}$$
$$V = \text{current}/\left(-\int_o^R \sigma\nabla\Phi 2\pi r\, dr\right). \quad (3)$$

Here, σ is the electrical conductivity of the gas, Φ is the scaled electric potential, $\vec{E}$ is the vector of the electric field strength, and $\vec{J}$ is the current density.

To compute the radiation source term, the RTE should be solved. An ordinary differential equation form of the RTE is expressed by (4). To solve the RTE, two approximations are used. First, the LTE is assumed, and second, the scattering effect is neglected [15]. An approximate RTE solution is obtained using a P-1 radiation model. In the P-1 radiation model, decompose the radiation intensity $I(r, s)$ into the position-dependent coefficients $I_l^m(r)$ and the spherical harmonics $Y_l^m(s)$ as expressed in (5)

$$-\frac{1}{\rho\kappa_v}\frac{dI_v}{ds} = I_v - B_v \quad (4)$$

$$I_v(r, s) = \sum_{l=0}^{\infty}\sum_{m=-l}^{l} I_l^m(r)Y_l^m(s). \quad (5)$$

In the above equations, κ_v is the absorption coefficient of the gas mixture and B_v is the Planck intensity as expressed by (11).

In the P-1 radiation model, the zeroth term and first term are left ($l = 1$) in the (5) as expressed in (6) and the radiation intensity can be expressed as (7). The detailed process of deriving the governing equations for the P-1 model is in [13]

$$I_v(r, s) = I_0^0 Y_0^0 + I_1^{-1} Y_1^{-1} + I_1^0 Y_1^0 + I_1^1 Y_1^1 \quad (6)$$

$$I_v(r, s) = \frac{1}{4\pi}(G_v + 3q_v \cdot s) \quad (7)$$

where G_v is the incident radiation and q_v in the radiative heat flux as (8)

$$G_v = \int_{4\pi} I_v(r, s)d\Omega, \quad q_v = \int_{4\pi} I_v(r, s)s\, d\Omega. \quad (8)$$

By combining (8) with (4) and integrating over solid angle Ω, The two equations can be obtained as (9)

$$\nabla \cdot q_v = 4\kappa_v\pi B_v - \kappa_v G_v, \quad \nabla G_v = -3\kappa_v q_v. \quad (9)$$

The final form of P-1 radiation model without scattering is expressed by (10)

$$\nabla \cdot (\Gamma\nabla G_v) - \kappa_v G_v + 4\pi B_v\kappa_v = 0(\Gamma = 1/3\kappa_v). \quad (10)$$

$$B_v = \frac{2h}{c^2}\frac{v^3}{e^{hv/k_B T} - 1}. \quad (11)$$

The total radiative heat source and the total radiative heat flux q_r are calculated by integrating the spectral radiative heat flux over band expressed by (12)

$$\nabla \cdot q_r = \sum_{i=1}^{N} 4\kappa_i\pi B_i - \kappa_i G_i. \quad (12)$$

Here, subscript i indicates the band number. These bands are described in detail in Section III.

III. NUMERICAL METHOD

A. AUSMPW+ Flux Scheme

In this paper, third-order spatial discretization is used for an accurate analysis. For the flux scheme, AUSMPW+ FVS scheme [1], [2] which is an improved type of AUSM, is used.

AUSMPW+ scheme can control the advection characteristic of the flow via the introducing a weighting function. The main advantage of AUSMPW+ scheme is its ability to control and remove oscillations near a wall or a shock. The numerical flux of AUSMPW+ is expressed as (13)

$$F_{\frac{1}{2}} = \overline{M_L^+} c_{\frac{1}{2}}\Phi_L + \overline{M_L^-} c_{\frac{1}{2}}\Phi_R + (P_L^+ P_L + P_R^- P_R) \quad (13)$$

where

$$\Phi = (\rho, \rho u, \rho v, \rho H, \rho_s)^T, \quad P = (0, p_x, p_y, 0)^T.$$

The subscripts $1/2$, L, and R represent the value at the cell-interface and on the left and right states across the cell-interface, respectively. Other variables in (13) are defined by (14)–(17)

1) $m_{1/2} \geq 0$

$$\overline{M_L^+} = M_L^+ + M_R^- \cdot [(1 - \omega) \cdot (1 + f_R) - f_L]$$
$$\overline{M_R^-} = M_R^- \cdot \omega \cdot (1 + f_R) \tag{14}$$

2) $m_{1/2} < 0$

$$\overline{M_L^+} = M_L^+ \cdot \omega \cdot (1 + f_L)$$
$$\overline{M_L^-} = M_L^- + M_R^+ \cdot [(1 - \omega) \cdot (1 + f_L) - f_R] \tag{15}$$

$$M^\pm = \begin{pmatrix} \pm \frac{1}{4}(M \pm 1)^2, & |M| \leq 1 \\ \frac{1}{2}(M \pm |M|), & |M| \leq 1 \end{pmatrix} \tag{16}$$

$$P^\pm = \begin{pmatrix} \frac{1}{4}(M \pm 1)^2(2 \mp M), & |M| \leq 1 \\ \frac{1}{2}(1 \pm \text{sign}(M)), & |M| > 1 \end{pmatrix}. \tag{17}$$

The pressure-based weight functions f and ω are given as

$$f_{L,R} = \left(\frac{p_{L,R}}{p_s} - 1 \right), \quad p_s \neq 0 \tag{18}$$

$$\omega(p_L, p_R) = 1 - \min \left(\frac{p_L}{p_R} \frac{p_R}{p_L} \right)^3 \tag{19}$$

where $p_s = P_L^+ p_L + P_R^- p_R$.

B. LU-SGS Time Iteration Scheme With a Dual-Time Stepping Method

Yoon and Jameson [4], [5] introduced an implicit algorithm based on lower–upper factorization and Gauss–Seidel relaxation. The LU-SGS scheme, which requires only scalar calculations for inversion, can reduce the memory usage and computation time considerably.

Equation (1) can be expressed using the residual term R as (20)

$$\frac{1}{J} \frac{dQ}{dt} + R(Q) = 0. \tag{20}$$

From (20), the term on the left side can be transformed by LU decomposition, as follows:

$$(LD^{-1}U)\Delta Q = -R \tag{21}$$

where

$$L = \frac{1}{J \Delta t} + D_\xi^- A^+ + D_\eta^- B^+ - A^- - B^- \tag{22-1}$$

$$D = \frac{1}{J \Delta t} + A^+ - A^- + B^+ - B^- \tag{22-2}$$

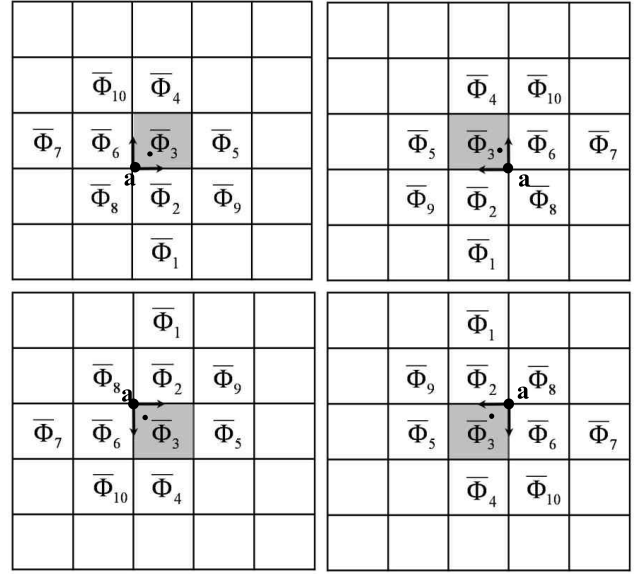$$U = \frac{1}{J \Delta t} + D_\xi^+ A^- + D_\eta^+ B^- - A^+ - B^+ \tag{22-3}$$

Fig. 1. Stencil cells for four cases according to the nearest point a from fringe cell (the upper right figure denotes case 1).

$$A^\pm = \frac{1}{2}(A \pm \rho(\overline{A})I) \tag{22-4}$$

$$B^\pm = \frac{1}{2}(B \pm \rho(\overline{B})I). \tag{22-5}$$

C. Fourth-Order Conservative Overset Method

The overset grid system has many advantages in the analysis of complex geometry and moving system, which are difficult to be examined by a single structured grid. In addition, it is easier to modify local parts of the geometry when the complex geometry changes, because no effort is required to regenerate the entire grid system except the changed parts. In this paper, fourth-order interpolation method [6], which can be applied to a high-order finite volume method (FVM) flow solver, is adopted. The interpolation process is divided into three steps.

1) Find fourth-order interpolation function in main grid:
In step 1, stencil cells are determined as the 10 nearest cells from the fringe cell and the interpolation function. Third-order interpolation function is as follows:

$$\Phi_m(\xi_m, \eta_m) = A\xi_m^3 + B\eta_m^3 + C\xi_m^2 \eta_m + D\xi_m \eta_m^2 + E\xi_m^2 + F\eta_m^2 + G\xi_m \eta_m + H\xi_m + I\eta_m + J. \tag{23}$$

To find the coefficients in (23), selection of six nearest cell from the fringe cell is needed. There are four cases of selecting stencil cells according to the location of the fringe cell center, as shown in Fig. 1.

After choosing stencil cells, the coefficients in (23) are obtained with each stencil cell satisfying (24) as follows:

$$\bar{\Phi}_m = \int_{\eta_i}^{\eta_{i+1}} \int_{\xi_i}^{\xi_{i+1}} \Phi_m(\xi_m, \eta_m) d\xi_m d\eta_m. \tag{24}$$

For case 1, the coefficients are obtained using (25), shown at the top of the next page.

$$
\begin{bmatrix} A \\ B \\ C \\ D \\ E \\ F \\ G \\ H \\ I \\ J \end{bmatrix} = \begin{bmatrix} 0 & 0 & -1/2 & 0 & 1/6 & 1/2 & -1/6 & 0 & 0 & 0 \\ -1/6 & 1/2 & -1/2 & 1/6 & 0 & 0 & 0 & 0 & 0 & 0 \\ 0 & 1 & -1 & 0 & 1/2 & 1/2 & 0 & -1/2 & -1/2 & 0 \\ 0 & 1/2 & -1 & 1/2 & 0 & 1 & 0 & -1/2 & 0 & -1/2 \\ 0 & -1/2 & 1/4 & 0 & 0 & -1/2 & 1/4 & 1/4 & 1/4 & 0 \\ 1/4 & -1/2 & 1/4 & 0 & 0 & -1/2 & 0 & 1/4 & 0 & 1/4 \\ 0 & -1 & 1 & 0 & 0 & -1 & 0 & 1 & 0 & 0 \\ 0 & 1/3 & 13/12 & -1/6 & -1/12 & -13/12 & 1/12 & -1/3 & 0 & 1/6 \\ 1/12 & -13/12 & 13/12 & -1/12 & -1/6 & 1/3 & 0 & -1/3 & 1/6 & 0 \\ -1/12 & 7/12 & 1/12 & 0 & 0 & 7/12 & -1/12 & 1/12 & -1/12 & -1/12 \end{bmatrix} \begin{bmatrix} \bar{\Phi}_1 \\ \bar{\Phi}_2 \\ \bar{\Phi}_3 \\ \bar{\Phi}_4 \\ \bar{\Phi}_5 \\ \bar{\Phi}_6 \\ \bar{\Phi}_7 \\ \bar{\Phi}_8 \\ \bar{\Phi}_9 \\ \bar{\Phi}_{10} \end{bmatrix}. \quad (25)
$$

Other cases are solved by rotating the coordinate of case 1.

2) Transform coordinates from the main grid to the overset grid:

In step 2, coordinate transformation from the main grid to the overset grid is done to obtain the value of Φ_o

$$
\begin{aligned}
\Phi_o(\xi_o, \eta_o) = & A'\xi_o^3 + B'\eta_o^3 + C'\xi_o^2\eta_o + D'\xi_o\eta_o^2 + E'\xi_o^2 \\
& + F'\eta_o^2 + G'\xi_o\eta_o + H'\xi_o + I'\eta_o + J'.
\end{aligned} \quad (26)
$$

The coefficient in (26) can be obtained using coordinate transformation using the chain rule.

3) Obtain the cell-averaged value of the fringe cell in the overset grid:

In step 3, the cell-averaged value $\bar{\Phi}_o$ is obtained by integrating the function $\Phi_o(\xi_o, \eta_o)$ written in (26).

D. Electric Potential Equation

The electric potential is used to obtain the electric field strength and Joule heating energy source by (3). The electric potential equation is a simple elliptic type equation and the point Gauss–Seidel iteration method is used to obtain electric potential value.

In this paper, a 2-D axisymmetric analysis is considered. Equation (2) can be written in the x, y coordinate via the following:

$$
\frac{\partial}{\partial x}\left(\sigma\frac{\partial\Phi}{\partial x}\right) + \frac{\partial}{\partial y}\left(\sigma\frac{\partial\Phi}{\partial y}\right) + \frac{1}{y}\frac{\partial\Phi}{\partial y} = 0. \quad (27\text{-}1)
$$

$$
\frac{\partial^2\Phi}{\partial x^2} + \frac{\partial^2\Phi}{\partial y^2} + \frac{1}{y}\frac{\partial\Phi}{\partial y} + \frac{1}{\sigma}\left(\frac{\partial\sigma}{\partial x}\frac{\partial\Phi}{\partial x} + \frac{\partial\sigma}{\partial y}\frac{\partial\Phi}{\partial y}\right) = 0. \quad (27\text{-}2)
$$

The form of point Gauss–Seidel iteration with a successive over relaxation method is expressed by (28)

$$
\begin{aligned}
\Phi_{i,j}^{k+1} = & \Phi_{i,j}^k - \frac{w}{d}F \\
F = & a\Phi_{i-1,j}^{k+1} + b\Phi_{i,j-1}^{k+1} + c\Phi_{i-1,j-1}^{k+1} \\
& + d\Phi_{i,j}^k + e\Phi_{i+1,j}^k + f\Phi_{i,j+1}^k \\
& + g\Phi_{i+1,j+1}^k + h\Phi_{i+1,j-1}^k + i\Phi_{i-1,j+1}^k. \quad (28)
\end{aligned}
$$

Terms of the first- and the second-order derivatives are mixed in (27-2). For the second-order derivative terms, the second-order central difference method is used, resulting in stable solutions. On the other hand, if the central difference method is also used for the first-order derivative terms, the nondiagonal terms in (28) become larger. This can cause instability by violating the diagonal dominance, especially when the electrical conductivity is very small or the gradient of electric conductivity is relatively large. To solve this problem, a selective difference method for enlarging the diagonal terms is used according to the gradient of the electric conductivity as follows.

1) The region where the gradient of the electric conductivity is positive

$$
\begin{aligned}
\left(\frac{\partial\sigma}{\partial x}\frac{\partial\phi}{\partial x}\right) = & \frac{\partial\sigma}{\partial x}\left\{\omega\left(\frac{\phi_{i+1,j} - \phi_{i,j}}{\Delta x}\right)\right. \\
& \left. + (1-\omega)\left(\frac{\phi_{i+1,j} - \phi_{i-1,j}}{2\Delta x}\right)\right\}. \quad (29)
\end{aligned}
$$

2) The region where the gradient of the electric conductivity is negative

$$
\begin{aligned}
\left(\frac{\partial\sigma}{\partial x}\frac{\partial\phi}{\partial x}\right) = & \frac{\partial\sigma}{\partial x}\left\{\omega\left(\frac{\phi_{i,j} - \phi_{i-1,j}}{\Delta x}\right)\right. \\
& \left. + (1-\omega)\left(\frac{\phi_{i+1,j} - \phi_{i-1,j}}{2\Delta x}\right)\right\}. \quad (30)
\end{aligned}
$$

A combination of a forward and a central difference method is used at the region where the gradient of the electric conductivity is positive, while a combination of a backward and a central difference method is used at the region where the gradient of the electric conductivity is negative. The weighting factor changes between 1 and 0, and the smoothly changing function according to the magnitude of the gradient of the electric conductivity as expressed by (31). The constant a in (31) is $60\,000$ and the constant C is 0.002 in this paper. Fig. 2 shows the computed weighting factor for given a temperature profile. As shown in Fig. 2, the central difference method is used at the center of the arc and near the wall while the first-order difference method is used at the edge of the arc

$$
\omega = C\max\left(\frac{\partial\log_a(1/\sigma)}{\partial x}, \frac{\partial\log_a(1/\sigma)}{\partial y}\right). \quad (31)
$$

E. P-1 Radiation Model

The P-1 radiation model transforms the RTE into a simple elliptic equation for incident radiation G. Therefore, the same algorithm used to solve the electric potential equation, the point Gauss–Seidel iteration method, can be used. Similar to (28), a 2-D axisymmetric form of the P-1 radiation model
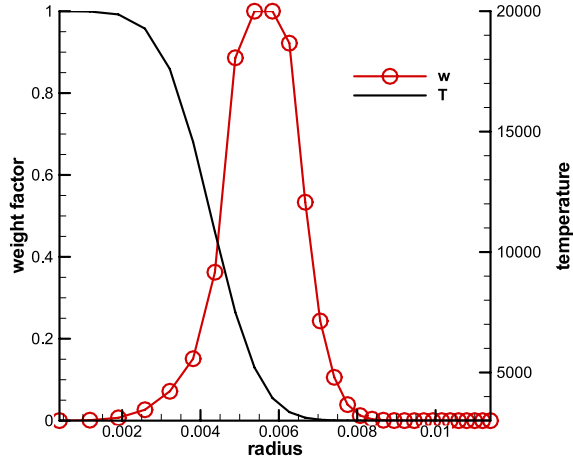
Fig. 2. Computed weighting factor for given temperature profile (at 1 bar).

Fig. 3. Averaged absorption coefficient compared with the actual absorption spectrum (at $T = 10\,000$ K and $p = 10$ bar).

without a scattering effect can be written in the x, y coordinate as follows:

$$\frac{\partial}{\partial x}\left(\Gamma\frac{\partial G}{\partial x}\right) + \frac{\partial}{\partial y}\left(\Gamma\frac{\partial G}{\partial y}\right) - \kappa G + 4\pi B_\nu \kappa = 0 \quad (32\text{-}1)$$

where

$$\Gamma = \frac{1}{3\kappa}. \quad (32\text{-}2)$$

The selective difference method is used according to the gradient of the absorption coefficient which is similar to solving the electric potential equation. Although the algorithm for solving the RTE is presented, there is another problem to be resolved before the radiative energy source term can be determined. Band averaging for SF_6 gas is required to obtain the effective absorption coefficients. In this paper, 11 bands based on the frequency are used. These bands are defined by (33) in units of 10^{15} Hz [7].

$$\nu_n = \{0, 0.2, .7, 1.77, 2.2, 2.5, 3.0, 3.5, 4.0, 4.5, 5.0, 10\}. \quad (33)$$

For the spectral averaging method, the Planck-averaging method is used. Planck-averaging overestimates the effective absorption coefficient at the peaks, and the substitution for the given limit values of the peaks is shown as follows [7]:

$$\kappa_\nu -> h(1 - e^{-\kappa_\nu \frac{1}{h}}). \quad (34)$$

Different limit values are applied considering the characteristic of the corresponding radiation bands. At low-frequency intervals, a limit value of h = 100(1/m) is used, while no limit value is used at high-frequency intervals. The averaged absorption coefficient in this paper is shown in Fig. 3 and is compared with the actual absorption spectrum.

F. Boundary Conditions

A no-slip boundary condition for the N-S equation is used at the wall. Thus, the normal component of the velocity must be zero and the tangential component of the velocity is identical to the speed of the moving parts. In addition, a change of the cell volume due to compression in the puffer cylinder is considered.
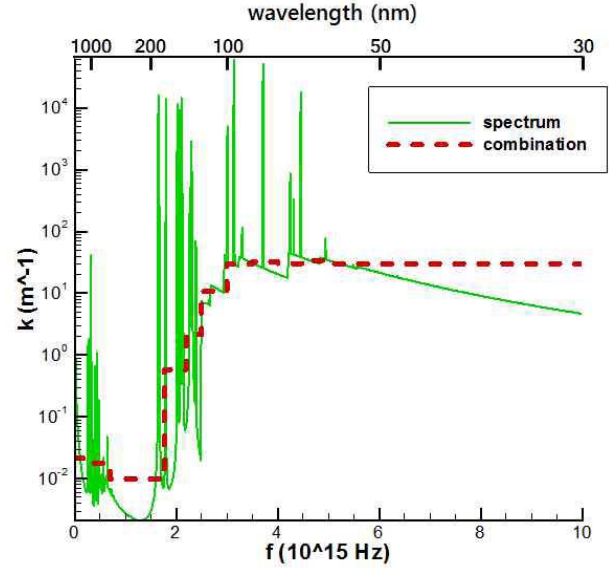
For the ablating wall, the rate of ablation is determined by (35)

$$q_r = \dot{m}h_v \quad (35)$$

where $\dot{m}$ is the ablation rate per area and h_v is the evaporation enthalpy of the PTFE. From the ablation rate, injection velocity of nozzle particle from the ablating wall can be determined. Evaporation temperature of the PTFE particles is set to 3400 K.

For the boundary conditions for the P-1 radiation model, a Marshak condition is used [10], [16] with wall emissivity of $\varepsilon_w = 1$. The Marshak condition is expressed by (36)

$$\frac{1}{\kappa}\vec{n} \cdot \nabla G = -\frac{3}{2}\frac{\varepsilon_w}{(2 - \varepsilon_w)}(G_w - 2\pi B). \quad (36)$$

IV. VALIDATION

In this section, validation of the numerical methods is done. Three validation cases are selected. First, two validation cases are analyzed to verify the boundary condition with a compression process through an analysis of the compression wave and cold gas flow computation. Second, the solution of the RTE is calculated using an arc temperature profile and compared with analytical results.

A. Compression Wave Analysis

An analysis of the compression wave and the determination of the pressure increment are possible if the speed of compression is constant or varies linearly. To verify the moving boundary condition and compressive process in the puffer cylinder, some case involving analytic solutions are tested in this paper. The flow conditions and moving conditions are shown in Fig. 4. The analytic solution of the pressure rise and the wave speed is calculated as (37) and (38). The detailed
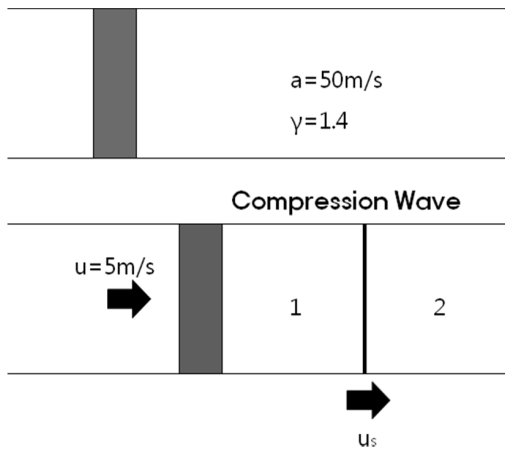
Fig. 4.   Conditions during the compressive process.

process of calculation is in [15]

$$\frac{p_2}{p_1} = \left[1 + \frac{1-\gamma}{2}\frac{|u_p|}{a_1}\right]^{\frac{2\gamma}{\gamma-1}} = 0.86812$$

$$\frac{\rho_2}{\rho_1} = \left[1 + \frac{1-\gamma}{2}\frac{|u_p|}{a_1}\right]^{\frac{2}{\gamma-1}} = 0.90392. \qquad (37)$$

$$u_s = u_p / \left(1 - \frac{\rho_2}{\rho_1}\right) = 52 \text{ m/s}. \qquad (38)$$

The numerical results are compared with analytic solutions, as shown in Fig. 5. The calculated increase in pressure and the wave speed are in good agreement with the analytic solution shown in Fig. 5.

B. Flow of Small Capacitive Current Breaking Analysis

A small capacitive current breaking analysis was conducted to verify the pressure rise due to compression. A puffer-type GCB is applied to the test case for verification. The entire mesh system for the flow analysis is shown in Fig. 6. An overset grid is used around a curve-shaped electrode. The overset layer of the main grid and the subgrid is shown in Fig. 7.

The pressure rise in the puffer cylinder is measured and calculated on the fixed wall in the puffer cylinder. Fig. 8 shows the result of the pressure rise in the puffer cylinder along with the date pertaining to the experimental pressure rise.

The value of the peak pressure rise shows a good agreement with the experimental data, while the time of peak pressure rise is delayed by 1–2 s. However, considering that there is also error in estimating the experimental data, the result shown in Fig. 8 can be considered as reliable.

C. Solution of the RTE

In this section, the solution of the RTE is calculated using the arc temperature profile by Tiemann and compared with the analytical results. The temperature profile is expressed by (39) and is shown in Fig. 9

$$T(r) = T_0 + \frac{1}{2}(T_a - T_0)\left[\text{erf}\left(\frac{\beta+r}{\alpha}\right) + \text{erf}\left(\frac{\beta-r}{\alpha}\right)\right]. \qquad (39)$$
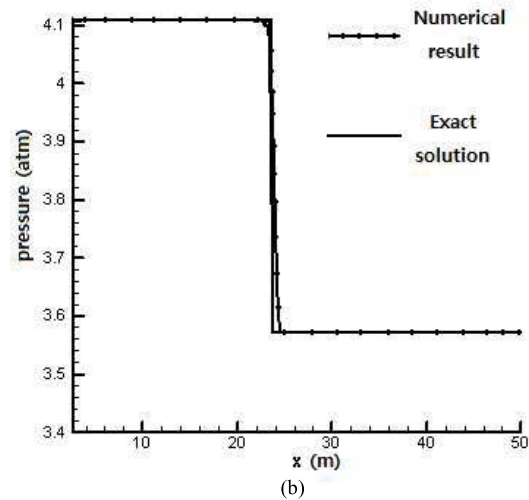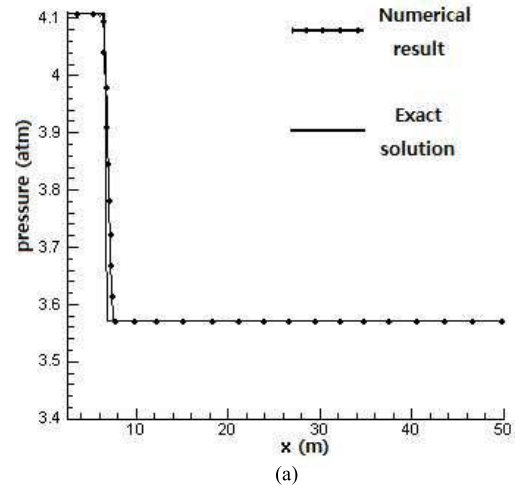

(a)

(b)

Fig. 5.   Pressure rise and wave speed. (a) At $t = 19$ s. (b) At $t = 43$ s.
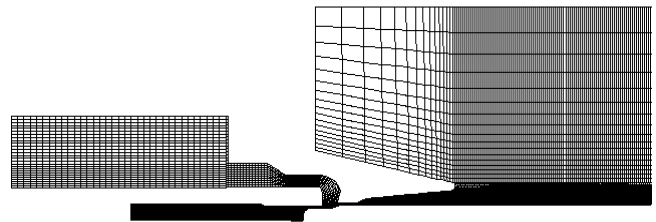

Fig. 6.   Mesh system for flow analysis.

For the validation axially blown arc is assumed in this case [7]. The radiative heat source is obtained by calculating the divergence of the radiation heat flux in (7).

Fig. 9 shows the radial profile of the radiative heat source calculated using P-1 radiation model and the exact solution.

It is known that Planck-averaging overestimates the emission [7]; however, the result using the limit length in Fig. 10 shows a fairly accurate solution.

V. NUMERICAL RESULTS

In this paper, a high-voltage self-blast circuit breaker is considered in the analysis. Simplified geometry of the self-blast circuit breaker is shown in Fig. 11.
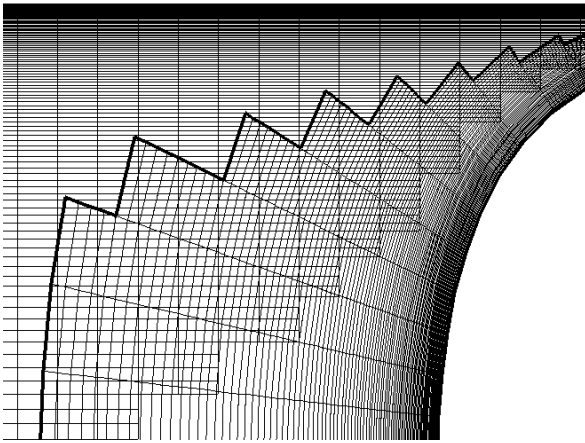
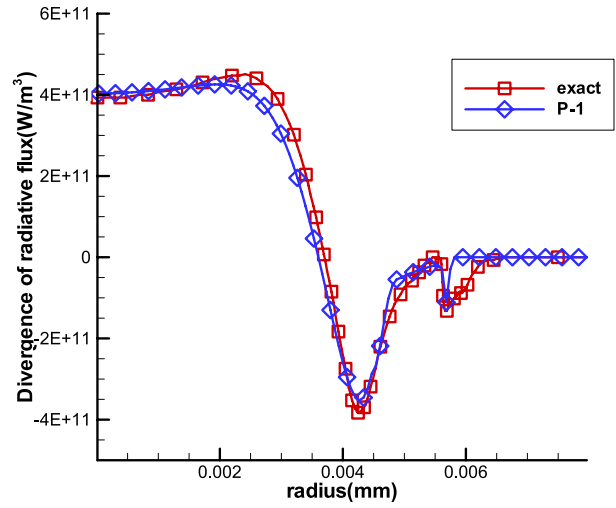Fig. 7.   Overset layer of each grid.

Fig. 8.   Pressure rise in the puffer cylinder.

Fig. 9.   Temperature profile by Tiemann (10 bar).

Fig. 10.   Divergence of the radiative heat flux of the P-1 model compared with the exact solution by Tiemann.

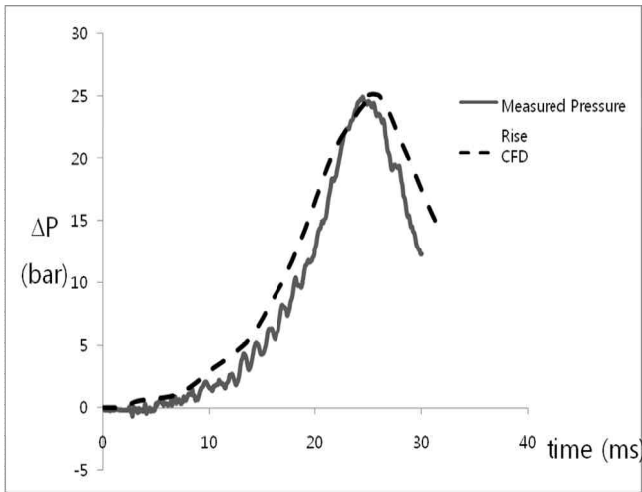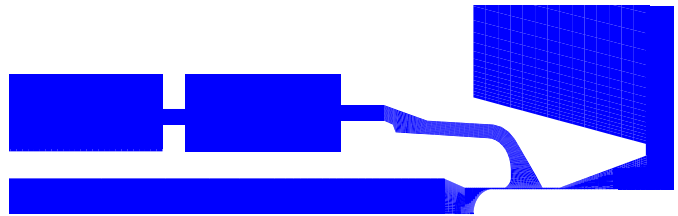Fig. 11.   Simplified geometry of a self-blast circuit breaker.
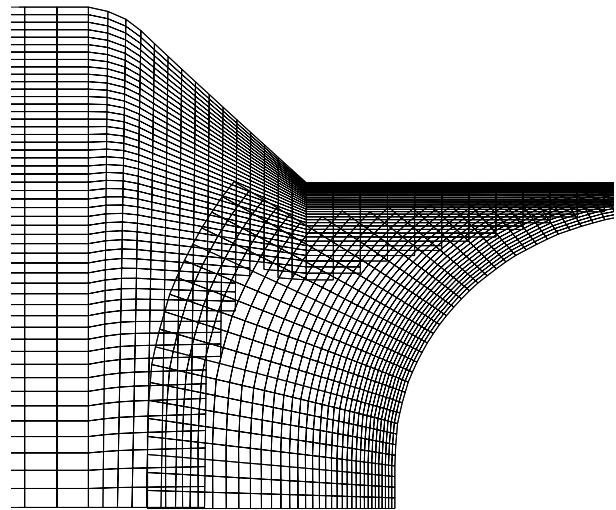

Fig. 12.   Overset layer of each grid after the hole searching process.

All blocks including the curve-shaped electrode consist of a structured grid. The overset grid method is used to represent both the nozzle and the curved electrode with a structured gird.

The overset layer of the main grid and the subgrid after the hole searching process are shown in Fig. 12. The grid of 200 points in the axial direction; 30 points in the radial direction are used for the main nozzle and 120 points in the axial direction and 30 points in the radial direction are used for the overset grid.
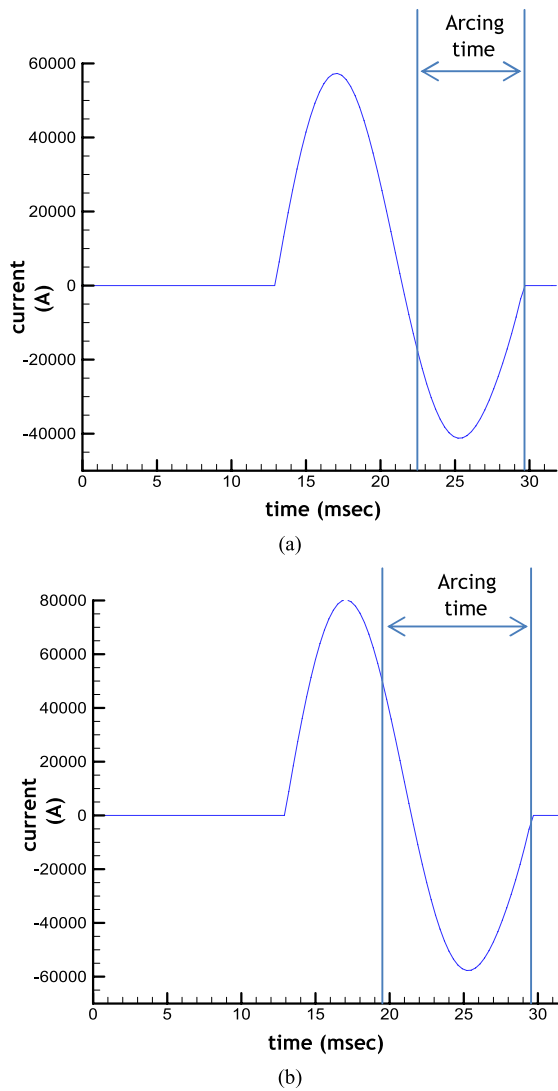
(a)

(b)

Fig. 13.   Current distribution of two cases. (a) Case a: arcing time 7.2 ms. (b) Case b: arcing time 10.4 ms.

The following two cases are analyzed with different arcing times of 7.2 and 10.4 ms. The current distributions of the two cases are shown in Fig. 13.

Fig. 13 shows that the wave forms of the two cases are identical while their current amplitudes and arcing times are different. The maximum current of the first case is ∼60 kA and the arcing time is ∼7.2 ms. In comparison, for the second case, the maximum current is ∼80 kA, which is larger than the current of the first case. The arcing time is ∼10.4 ms, which is longer than that of the first case. The particular difference from the first case is that the second case has a current-zero point during the arcing time. This can produce a complicated curve of the pressure rise, such as when the pressure decreases at the current zero.

A. Electric Field Analysis

The electric field is considered only in the main nozzle part of the circuit breaker. Fig. 14 shows the result of the electric field analysis. A moving contact and a fixed contact are set as
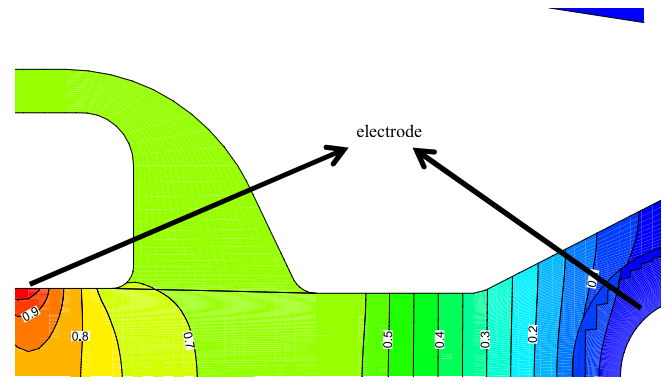

Fig. 14.   Electric field around electrodes.
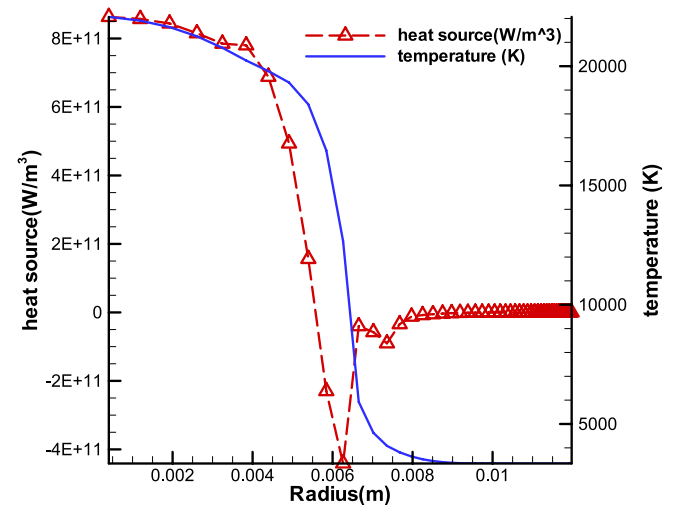

Fig. 15.   Divergence of the radiative flux along the radial direction at the nozzle.

the electrode, and Fig. 14 shows that the electric current flows from one electrode to the other.

B. Radiative Source Analysis

The radiation source term, which can also be represented as the divergence of the radiative flux, is calculated at the nozzle throat. Fig. 15 shows the temperature profile and the divergence of the radiative flux at 20 ms. The radiative source has a maximum value at the center of the arc, while reabsorption occurs at the edge of the arc.

C. Pressure Rise in the Expansion Chamber

A heat gas flow analysis was conducted for the two cases. The increase in the pressure was measured by both an experiment and calculation at the wall in the expansion chamber. The results are shown in Fig. 16 and are compared with the experimental data. An arc is created at ∼22 ms in the first case and at 19 ms in the second case.

For the first case, the value of the peak pressure and the time taken to reach the peak pressure are well matched with the experimental results, as shown in Fig. 16(a). It can be observed in Fig. 16(b) that a pressure jump occurs in the experimental data at 17 ms while the numerical result shows a
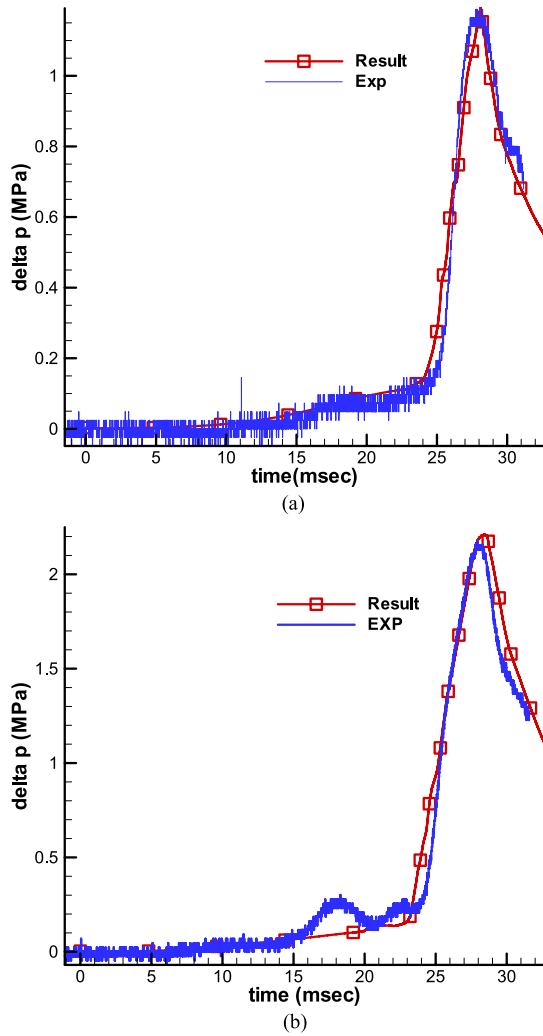
Fig. 16. Pressure rise in the expansion chamber compared with the experimental result. (a) Arcing time: 7.2 ms. (b) Arcing time: 10.4 ms.

TABLE I
CALCULATED PRESSURE COMPARED WITH THE EXPERIMENTAL
DATA, ARCHING TIME: 7.2 ms

	CFD	EXP	Err
Peak pressure(MPa)	1.207	1.183	2.0%
Peak pressure time(msec)	28.11	27.78	1.2%
Pressure rise at current zero	0.917	0.990	7.3%

TABLE II
CALCULATED PRESSURE COMPARED WITH THE EXPERIMENTAL
DATA, ARCHING TIME: 10.4 ms

	CFD	EXP	Err
Peak pressure(MPa)	2.239	2.172	3.0%
Peak pressure time(msec)	28.42	28.06	1.3%
Pressure rise at current zero	1.926	1.657	13.9%

the wall in the expansion chamber. The experimental data has a tendency to oscillate at the maximum pressure point; therefore, the mean value is calculated and used. The value of the peak pressure and the time of the peak pressure in both the cases are in agreement with the experimental data except for the pressure value at the current zero. The pressure error at the current zero is larger than 10% for the second case. For several cases, the calculation has not been done after the current zero because the pressure values do not match the experimental data. It is known that the arc behavior at the current zero is mainly influenced by turbulence at the edge of the arc. An appropriate turbulence model is required for an accurate calculation at the current zero and after this point.

VI. CONCLUSION

In this paper, code development using an overset grid method is used to determine the internal flow of a self-blast circuit breaker. The overset method with fourth-order interpolation and a third-order spatial discretization method were used for an accurate analysis. In addition, calculations of the electric field, radiation, and nozzle ablation were considered. For the electric field and P-1 radiation calculations, a new difference method to solve an elliptic-type equation was introduced. For validation, a test of compression process and small capacitive current breaking case were selected and used. The P-1 radiation model was used to obtain a solution to the RTE, and this was validated by comparing it with the solution using the Tiemann profile. Several flow cases in a high-voltage self-blast circuit breaker were analyzed using a structured grid. The numerical result of the pressure rise agreed well with the experimental data.

monotonic rise. Although the electrodes are detached and the arc is created at ~19 ms, the pressure jump in the experimental data is inexplicable. One possible explanation is noise error, especially when the current amplitude reaches its maximum point. The value of the peak pressure, and the time of the peak pressure of the second case are also in good agreement with the experimental results, as shown in Fig. 16(b).

Tables I and II show the results of the pressure rise and the error between the experimental data and the calculated value at

REFERENCES

[1] K. H. Kim, J. H. Lee, and O. H. Rho, "An improvement of AUSM schemes by introducing the pressure-based weight function," *Comput. Fluids*, vol. 27, no. 3, pp. 311–346, 1998.
[2] K. H. Kim, C. Kim, and O. H. Rho, "Methods for the accurate computations of hypersonic flows—Part I: AUSMPW+scheme," *J. Comput. Phys.*, vol. 174, no. 1, pp. 38–80, 2001.
[3] S. H. Yoon, C. Kim, and K. H. Kim, "Multi-dimensional limiting process for three-dimensional flow physics analyses," *J. Comput. Phys.*, vol. 227, no. 12, pp. 6001–6043, 2008.

[4] S. K. Yoon and A. Jameson, "Lower-upper symmetric-Gauss-Seidel method for the Euler and Navier-Stokes equations," *AIAA J.*, vol. 26, no. 9, pp. 1025–1026, 1988.

[5] A. Jameson and S. Yoon, "LU implicit schemes with multiple grids for the Euler equations," in *Proc. AIAA 24th Aerosp. Sci. Meeting*, 1986, pp. 1–12.

[6] K. L. Lee, J. H. Park, and K. H. Kim, "High order interpolation method for overset grid based on finite volume method," *AIAA J.*, vol. 49, no. 7, pp. 1387–1398, 2011.

[7] H. Nordborg and A. A. Iordanidis, "Self-consistent radiation based modeling of electric arcs: I. Efficient radiation approximations," *J. Phys. D, Appl. Phys.*, vol. 41, no. 13, pp. 1–10, 2008.

[8] L. S. Frost and R. W. Liebermann, "Comparison and transport properties of SF_6 and their use in a simplified enthalpy flow arc model," *Proc. IEEE*, vol. 59, no. 4, pp. 474–485, Apr. 1971.

[9] C. M. Dixon, J. D. Yan, and M. T. C. Fang, "A comparison of three radiation models for the calculation of nozzle arcs," *J. Phys. D, Appl. Phys.*, vol. 37, no. 23, pp. 3309–3318, 2004.

[10] S. D. Eby, J. Y. Trepanier, and X. D. Zhang, "Modelling radiative transfer in SF_6 circuit-breaker arcs with the P-1 approximation," *J. Phys. D, Appl. Phys.*, vol. 31, no. 13, pp. 1578–1588, 1998.

[11] H. K. Kim, K. Y. Park, C. H. Im, and H. K. Jung, "Optimal design of gas circuit breaker for increasing the small current interruption capacity," *IEEE Trans. Magn.*, vol. 39, no. 3, pp. 1749–1752, May 2003.

[12] V. Aubrecht and B. Gross, "Net emission coefficient of radiation in SF_6 arc plasma," *J. Phys. D, Appl. Phys.*, vol. 27, no. 1, pp. 95–100, 1994.

[13] M. F. Modest, *Radiative Heat Transfer*. San Francisco, CA, USA: Academic, 2003.

[14] R. I. Souloukhin, *Handbook of Radiative Heat Transfer in High-Temperature Gases*. New York, NY, USA: Hemisphere, 1987.

[15] L. D. Landau and E. M. Lifshitz, *Fluid Mechanics*. New York, NY, USA: Pergamon, 1959.

[16] R. Siegel and J. R. Howell, *Thermal Radiation Heat Transfer*. New York, NY, USA: Hemisphere, 1992.

[17] M. S. Liou and K. H. Kao, "Progress in grid generation: From chimera to DRAGON grids," NASA, Washington, DC, USA, Tech. Memo. 106709, 1994.

[18] R. P. Hansen and J. R. Forsythe, "A comparison of structured and unstructured grid solutions for flow over a circular cylinder," in *Proc. DoD User Group Conf.*, 2003, pp. 103–112.

Kyu Hong Kim was born in Seoul, Korea, on November 30, 1972. He received the B.S. and M.S. degrees in aerospace engineering from Seoul National University, Seoul, in 1995 and 1997, respectively, and the Ph.D. degree in hypersonic and rarefied gas flow from Seoul National University in 2001.

He is currently a Professor of aerospace engineering with Seoul National University.

Dr. Kim is a member of AIAA.

Chang Ho Yeo was born in Korea, in 1976. He received the B.S. and M.S. degrees in mechanical engineering from Dong-A University, Busan, Korea, in 2003 and 2005, respectively.

He has been involved in development of self-blast puffer type circuit breaker with HYOSUNG Corporation, Seoul, Korea, since 2006. He is interested in analysis of the thermal, fluid in circuit breaker. His current research interests include computational fluid dynamics of arc plasma and temperature rise.

Jung Ho Park (S'13) was born in Seoul, Korea, on June 22, 1983. He received the B.S. degrees in aerospace engineering from Seoul National University, Seoul, in 2006. Currently, he is pursuing the Ph.D. degree.

He is a student member of AIAA.

Hong Kyu Kim was born in Yeongchon, Korea, in 1969. He received the B.Sc., M.Sc., and Ph.D. degrees from the School of Electrical Engineering, Seoul National University, Seoul, Korea, in 1995, 1997, and 2001, respectively.

He has been with the Korea Electrotechnology Research Institute, Ansan, Korea, since 2001. His current research interests include the numerical analysis of electromagnetic fields, and the analysis of cold and hot gas flow in high voltage gas circuit breakers.

Dr. Kim is a regular member of the CIGRE Working Group A3.24.